

## RESEARCH ARTICLE

10.1002/2014JD023014

## Key Points:

- Orographic precipitation enhancement varies little between 33°S and 44°S
- Orographic effects on rainy clouds increase from midlatitudes to subtropics
- Ice water path is largest in rainy clouds upstream of the tall subtropical Andes

## Correspondence to:

M. Viale,  
maxiviale@mendoza-conicet.gob.ar

## Citation:

Viale, M., and R. Garreaud (2015), Orographic effects of the subtropical and extratropical Andes on upwind precipitating clouds, *J. Geophys. Res. Atmos.*, 120, doi:10.1002/2014JD023014.

Received 19 DEC 2014

Accepted 17 APR 2015

Accepted article online 21 APR 2015

## Orographic effects of the subtropical and extratropical Andes on upwind precipitating clouds

Maximiliano Viale<sup>1</sup> and René Garreaud<sup>1</sup>
<sup>1</sup>Departamento de Geofísica, Facultad de Ciencias Físicas y Matemáticas, Universidad de Chile, Santiago, Chile

**Abstract** The orographic effect of the Andes (30°S–55°S) on upwind precipitating clouds from midlatitude frontal systems is investigated using surface and satellite data. Rain gauges between 33°S and 44°S indicate that annual precipitation increases from the Pacific coast to the windward slopes by a factor of  $1.8 \pm 0.3$ . Hourly gauges and instantaneous satellite estimates reveal that the cross-barrier increase in annual precipitation responds to an increase in both the intensity and frequency of precipitation. CloudSat satellite data indicate that orographic effects of the Andes on precipitating ice clouds increase gradually from midlatitudes to subtropics, likely as a result of a reduction of synoptic forcing and an increase of the height of the Andes equatorward. To the south of 40°S, the thickness of clouds slightly decreases from offshore to the Andes. The total ice content increases substantially from the open ocean to the coastal zone (except to the south of 50°S, where there is no much variation over the ocean), and then experience little changes in the cross-mountain direction over the upstream and upslope sectors. Nevertheless, the maximum ice content over the upslope sector is larger and occurs at a lower level than their upwind counterparts. In the subtropics, the offshore clouds contain almost no ice, but the total and maximum ice content significantly increases toward the Andes, with values being much larger than their counterparts over the extratropical Andes. Further, the largest amounts of cloud ice are observed upstream of the tallest Andes, suggesting that upstream blocking dominates there.

## 1. Introduction

Frontal precipitation systems rooted in midlatitude cyclones are profoundly altered when moving over major mountain ranges [e.g., Roe, 2005; Houze, 2012], often producing orographic precipitation enhancement over the windward slopes of the mountains and a rain shadow to their lee. The intensity and upstream extent of the orographic enhancement are highly dependent on both the mountain geometry (especially its height and width) and environmental conditions (especially the impinging moist flow and stability) as demonstrated in multiple observational and theoretical studies [e.g., Medina and Houze, 2003; Bousquet and Smull, 2003; Colle, 2004; Galewsky, 2008; Neiman et al., 2002, 2009]. An archetypical setting for stratiform orographic precipitation is the southern sector of the Andes, running for about 3000 km near the west coast of southern South America (Figure 1). The Andes mean height surpasses 4000 m above sea level (asl) at subtropical latitudes (25°S–35°S), then rapidly decreases southward, reaching less than 1500 m asl in its southern portion (40°S–55°S) except for a few isolated peaks in excess of 3000 m asl. On the other hand, the Andean width is less than 200 km at subtropical latitudes and increases farther south up to about 400 km forming an elevated plateau.

Orographic effects of the subtropical Andes on frontal precipitation have been more explored than those of the extratropical Andes, largely because observations are comparatively more sparse farther south (as detailed below). Climatological approaches using surface and rawinsonde observations have documented a precipitation enhancement over the relatively dry ( $<1000$  mm/yr) windward slopes of the subtropical Andes during the passage of cold fronts [Falvey and Garreaud, 2007; Viale and Nuñez, 2011] and more markedly during warm winter storms [Garreaud, 2013]. Further airflow analyses from case studies revealed that blocked low-level poleward winds intensify convergence on the equatorward moving front [Barrett et al., 2009], forcing the midlevel westerly flow to rise before the barrier. The forced uplift produces a midlevel cloud deck with ice particles, which in turn, interact with the approaching front and enhance precipitation upstream of the barrier [Viale et al., 2013].

The extratropical Andes locate in the remote Patagonia region, where their upstream sector features inaccessible islands and sparsely populated terrain with virtually nonexistent surface stations. Mean annual

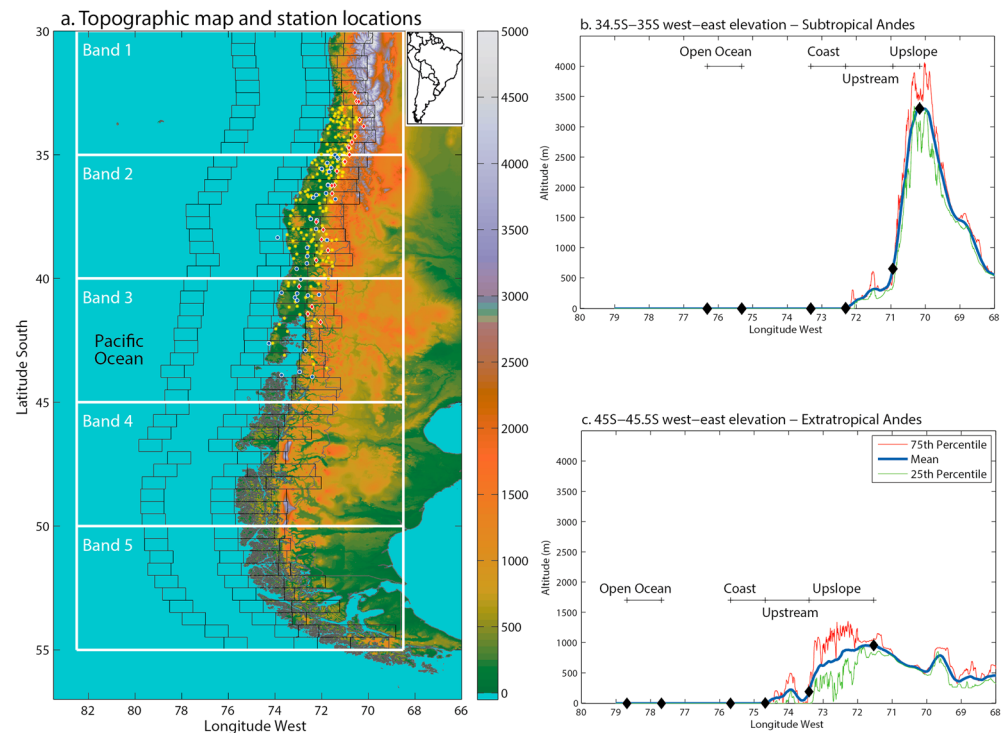


**Figure 1.** (a) The study region over the west coast of the southern South America with the daily (yellow asterisks) and hourly (blue circles) rain gauges and the stream gauges (red diamonds) data sets. To illustrate the criterion used to define the open ocean, coast, upstream, and upslope cross-barrier zones within  $0.5^\circ$  width black rectangles in Figure 1a, two meridionally averaged east-west cross section of the Andes mean altitude (blue line) and 25th and 75th percentile altitude (green and red lines) are presented for the (b)  $35^\circ\text{S}$ – $34.5^\circ\text{S}$  and the (c)  $45^\circ\text{S}$ – $45.5^\circ\text{S}$  latitudinal bands, representative of the subtropical and extratropical Andes, respectively. The thick white rectangles in Figure 1a represent the  $5^\circ$  width latitudinal bands used for grouping vertical profiles from the CloudSat data set.

precipitation in this sector is above 3000 mm. Understandably, the few existent climatological approaches to orographic precipitation in the extratropical Andes has been based on long-term numerical simulation [Garreaud *et al.*, 2013; Lenaerts *et al.*, 2014] or on indirect estimates, such as stable isotope data from stream water [Smith and Evans, 2007] or lightning activity data [Garreaud *et al.*, 2014]. Nonetheless, there is clear evidence for a marked precipitation enhancement to the west of the extratropical Andes.

In the present study we aim at characterizing the orographic effects of the Andes (south of  $30^\circ\text{S}$ ) on upwind precipitating clouds by using surface and CloudSat satellite observations (see details in section 2). A brief climatological background in precipitation along the Andes is presented in section 3. Rain gauges with daily and hourly records allow a first-order estimation of the rainfall increase from the coast toward the mountains at different latitudes (section 4). The multiyear satellite data set is then used to characterize macrophysical and microphysical properties of precipitating clouds to the west of the crest of the subtropical and extratropical Andes (section 5) helping to interpret the surface observations and compare the orographic effects in the two different sectors of the Andes (semiarid and high versus hyperhumid and low). Discussion and main results are summarized and in sections 6 and 7, respectively.

## 2. Data and Methodology

### 2.1. Surface Data

Figure 1a shows the location of the precipitation stations used in this study superimposed on a topographic map of the west coast of southern South America. Two types of data sets are available. The daily precipitation (accumulations at 12:00 UTC = 09:00 LT) data set consists of 216 stations with a 10 year long record (2002–2011) managed by the Chilean Agency of Water (Dirección General de Aguas (DGA)). There are no stations to the west of the Andes to the south of  $45^\circ\text{S}$  due to the inaccessibility and remoteness of

that sector. The hourly precipitation data set consists of 47 automatic stations, 35 of them managed by the Chilean Department of Agriculture (AGROMET) and 12 of them installed by the authors, both data sets covering from April 2013 to August 2014. Because the AGROMET stations are located mostly on the central valley west of the Andes, we installed our stations in five east-west transects (at 36°S, 38°, 40°, 42°, and 44°S) from the coast to the upslope sector of the Andes. For both data sets, we retained stations with less than 10% of missing values and located below 2000 m, since the rain gauges were not suited to measure snow (the only exception was station Lagunitas at 2765 m near Santiago because it provides reliable daily rain and snow measurements).

Reliable mean annual river discharges from 22 streamflow gauges over a 20 year period (1985–2005) were used to estimate long-term mean annual precipitation (MAP) in Andean drainage basins (33°S–44°S). River gauges provide a rough estimate of the upper bound of MAP over the windward slope of the Andes (where rain gauges are almost inexistent), since the simple water balance calculation neglect evapotranspiration and groundwater runoff, and the basins have their headwaters in the continental divide. MAP was estimated using a simple water balance ( $MAP = Q/A$ , where  $Q$  is the annual mean streamflow and  $A$  is the drainage area;  $Q$  and  $A$  were obtained from the DGA following the procedure similar to the employed in *Falvey and Garreaud* [2007]).

## 2.2. Satellite Data

In order to characterize properties of precipitating clouds, we use CloudSat and CALIPSO satellite data. Unlike the surface precipitation data, the satellite products extend over the entire extratropical range allowing a comparison between the clouds systems upwind of the subtropical and extratropical Andes. CloudSat has a Cloud Profiling Radar (CPR) sensor [*Im et al.*, 2005] that is sensitive to cloud and precipitation particles; CALIPSO has a cloud-aerosol lidar sensor (Cloud-Aerosol Lidar with Orthogonal Polarization (CALIOP)) [*Winker et al.*, 2009] and is more sensitive to thin clouds that could be missed by the CPR. The two polar-orbiting satellites flew with tight formation from April 2006 to April 2011 in NASA's A-Train constellation [*Stephens et al.*, 2002], enabling the overlap of the radar and lidar footprints. After a battery anomaly of the CloudSat spacecraft in April 2011, CloudSat retrieves data only in the sunlight portion of the orbit and can no longer maintain tight formation with CALIPSO. The horizontal resolution of the CPR footprint is 1.7 km (cross track) by 1.3 km (along track), and the profiles have 125 vertical bins of reflectivity factor with 240 m gate spacing from the surface to near 30 km height. The lidar has higher spatial resolution than the CPR, but the spatial domain of the CPR-LIDAR combined products is defined in terms of the spatial grid of the CPR.

More than 7 years (2007–2014) of CloudSat radar only data and almost 4 years (2006–2011) of CloudSat-CALIPSO-combined radar lidar data were analyzed over the west coast of South America. The organization in space of the data is explained in the next subsection. For the purpose of this study, only rainy vertical profiles were analyzed. A rainy profile was identified by using the precipitation flags within the 2C-PRECIP-COLUMN product, where flag values with high confidence for precipitation was considered. Insight of the macrophysical and microphysical properties of precipitating clouds was gained by analyzing the cloud top heights, as well as the ice content parameters available in the 2B-GEOPROF-LIDAR [*Mace et al.*, 2009] and the 2B-CWR-RO [*Austin et al.*, 2009] products, respectively.

Two important issues of the CloudSat data have been considered in the analysis of rainy profiles. The CPR radar sensitivity detects clouds rather than precipitation (unlike typical weather radar), and the near-surface signal can be attenuated under a rainy situation due to the absorption or multiscattering by hydrometeors with large liquid water content [*Mace et al.*, 2007; *Marchand et al.*, 2008]. As a result, the liquid content parameters in the CWC-RO product have ~90% missing values of all rainy profiles; in fact, the level of attenuation is used as a source of information to estimate rainfall over the Oceans [*Haynes et al.*, 2009]. The other issue is the surface clutter contamination which largely limits the signal below ~0.5 km over the ocean surface and below ~1.5 km over the land surface. To deal with these issues, we restrict our analysis to ice content and cloud top height parameters representative of the middle and upper portions of the cloud layers.

## 2.3. Grouping Observational Data in Cross-Barrier Zones and Latitudinal Bands

To examine the first-order influence of the Andes on precipitation, we took advantage of the nearly two dimensional structure of this mountain range with a north-south direction approximately (Figure 1). To this effect, we considered a sequence of zonal transects extending from the Pacific Ocean to the Andes ridge.

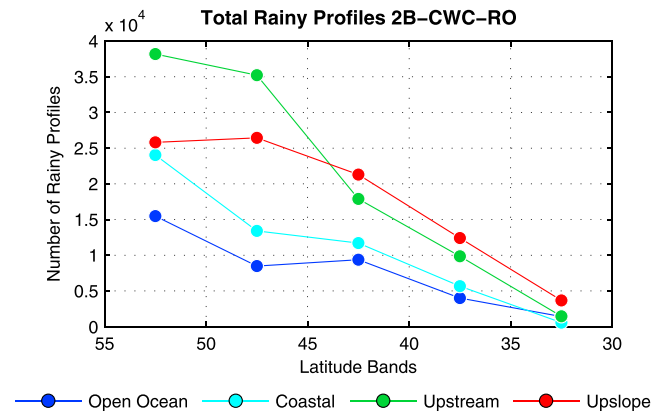


**Figure 2.** Numbers of rainy profiles available in the 2B-CWC-RO product over the 2006–2014 period. The satellite data set was grouped in 5° width latitude bands and cross-barrier zones (see text for details).

The transects do not overlap, have a width of 0.5° of latitude, and cover from 30°S to 55°S (Figure 1). In each transect, we define a mean zonal profile of the Andes taking the meridional average of a high resolution digital elevation model (GTOPO-30 s) and find the longitude and altitude of the crest (highest point). We then subdivide each transect in four cross-barrier zones from the crest of the Andes to the open ocean (Figures 1b and 1c): upslope, upstream, coastal, and open ocean. The upslope zone extends from the crest to the (western) foothill, defined as the point with height equal to a quarter of the crest within each transect. The upstream zone extends from the foothill to the coastline (identified by the mean transect height equal to zero), thus including the low terrain where most of Chilean cities are located. According to the theoretical radius of deformation [Pierrehumbert and Wyman, 1985], the upstream orographic influences on the flow could extend to ~600 km away of the tallest Andes crestline [e.g., Viale et al., 2013]. Therefore, we define the coastal and open ocean zones as the parts of the transect extending westward from the coastline to 100 km and from 300 to 400 km offshore, respectively. Thus, the open ocean zones are located more than ~600 km away from the Andes crest and are virtually immune to orographic effects.

Each surface station and satellite-based profile were grouped according to its cross-barrier and latitudinal location, using the four zones defined before. Note that this grouping does not consider the actual elevation of the station or the satellite footprint but rather the 0.5° meridionally averaged topographic profile. Previous studies have pointed out that the relationship between precipitation and altitude is improved when considering the surrounding elevation instead of the specific elevation of the station [e.g., Rasmussen and Tangborn, 1976; Frei and Schär, 1998; Falvey and Garreaud, 2007].

When analyzing the satellite profiles, we grouped the 0.5° latitude transects in five latitudinal bands of 5° each to ensure a good sample size to calculate statistics (i.e., in the area enclosed by white rectangles in Figure 1a). The number of satellite-based rainy profiles available over each zone ranged from 700 to 1000 in the northernmost band to  $1.5\text{--}3 \times 10^4$  in the southernmost band over the whole period (2007–2014) for the CWC-RO product (Figure 2). It should be noted that the big differences in the number of profiles arise from the differences in the precipitation occurrences (as we detailed below) and from the slightly different widths of the upstream and upslope zones. For the GEOPROF-LIDAR product, a general reduction of ~30% is observed everywhere due to the shorter period (not shown).

### 3. Latitudinal Variation in Long-Term Precipitation

Before focusing on cross-barrier variations in precipitation and cloud properties, we provide in this section a brief climatological background of the latitudinal (approximately along barrier) variation in the precipitation using the 10 year (2002–2011) long records of daily rain gauge data from 33°S to 44°S. For each station, we calculated the annual mean accumulation ( $R_m$ ), the percentage of rainy days ( $R_f$ , daily accumulation > 0 mm) relative to the total days with available data, as well as the median and the 25th and 75th percentile values of the daily accumulation when rain is present (i.e., representative of the precipitation intensity at daily time scale,  $R_i$ ). Using these calculations, we explore how much of the along- and cross-barrier (next section) variation in  $R_m$  is determined by variations in  $R_f$  and  $R_i$ , since the amount of precipitation can be decomposed into frequency and intensity [e.g., Rotunno and Ferretti, 2001; Yuter et al., 2011; Biasutti and Yuter, 2013].

A marked southward increase in  $R_m$  is observed (Figure 3a), ranging from ~500 mm at subtropical latitudes (to the north of 35°S) to more than 2000 mm at midlatitudes (south of 39°S). The southward increase in

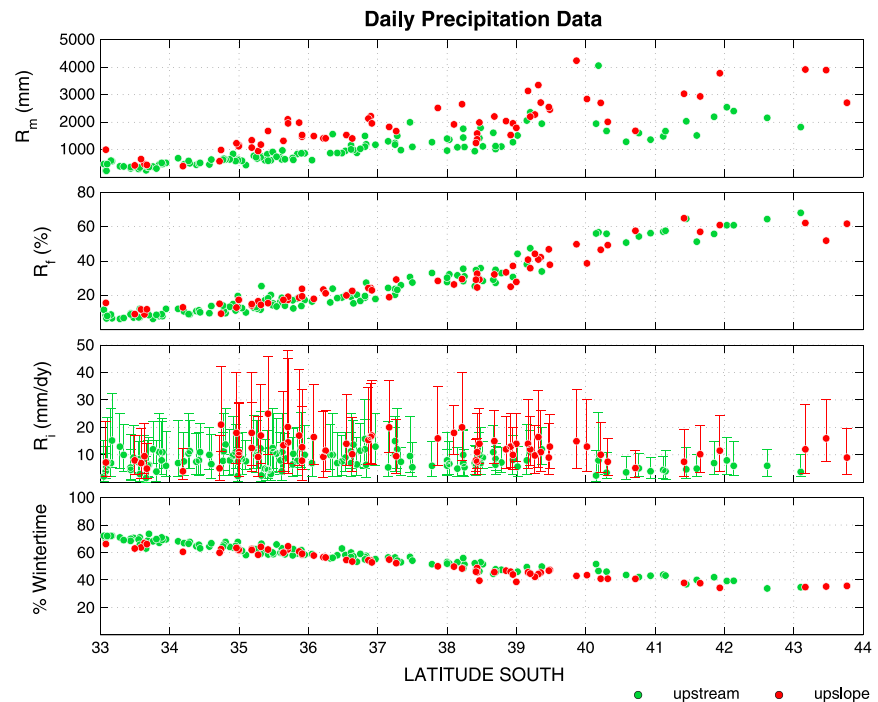


**Figure 3.** Scatterplot of several variables versus latitude using surface daily precipitation data set. The variables are (a) annual mean precipitation (millimeter), (b) frequency (%), (c) intensity of precipitation ( $\text{mm d}^{-1}$ ), presented by errorbars with the median (circles) and 25th and 75th percentile limit (barbs) values, and (d) the percentage of wintertime (June–July–August) precipitation of the annual total (%). The green and red colors indicate stations located in the upstream and upslope cross-barrier sectors, respectively.

annual mean rainfall is primarily determined by a southward increase in the frequency of rainy days ( $R_f$ ; Figure 3b) rather than variation in intensity of rainy days ( $R_i$ ; Figure 3c). Considering the whole set of rain gauge stations, the correlation between  $R_m$  and  $R_f$  is 0.83 and between  $R_m$  and  $R_i$  only 0.4. In fact,  $R_i$  slightly reduces southward regardless of the location in the zonal transect, a feature that could be related to the poleward decrease of precipitable water and of the height of the Andes. Note that cross-barrier variations in  $R_m$  and  $R_f$  at the same latitude are also distinguishable in Figures 3a and 3c. Another feature of precipitation closely related to the latitude is its seasonality. Wintertime (June, July, and August) precipitation accounts for more than 70% of the annual accumulation to the north of 35°S, where the subtropical anticyclone over the SE Pacific precludes the arrival of cold fronts during most of the year [e.g., Rutllant and Fuenzalida, 1991]. To the south of 40°S, the precipitation is more evenly distributed through the year, and yet wintertime rainfall accounts for about 40% of the annual total due to the seasonal strengthening of the storm track around 50°S [e.g., Hoskins and Hodges, 2005]. Summer convection is restricted to the elevated terrain and accounts for less than 10 % of annual total precipitation over the western slope of the subtropical Andes [Viale and Garreaud, 2014].

#### 4. Orographic Effects on Upwind Precipitation Inferred From Surface Data

In this section, we focus on the cross-barrier variation in precipitation, considering either daily or hourly data for the annual mean accumulation ( $R_m$ ), frequency ( $R_f$ ), and intensity ( $R_i$ ).

##### 4.1. Annual Mean Precipitation

Figure 4 shows the annual mean rainfall accumulation in zonal transects of 1° of latitude each. The stations are differentiated according to their location in the upstream or upslope zones following the procedure described in section 2.3. The orographic enhancement of  $R_m$  over the western side of the Andes is evident in the sampled transects, and the ratios of  $R_m$  over the upslope zone to those over the upstream zone are all greater than one (Table 1). Considering the Andes between 33°S and 44°S, the mean orographic enhancement ratio results  $1.79 \pm 0.32$  (i.e., the mean ratio of  $R_m$  estimated on upslope zones to  $R_m$  estimated on upstream zones). The

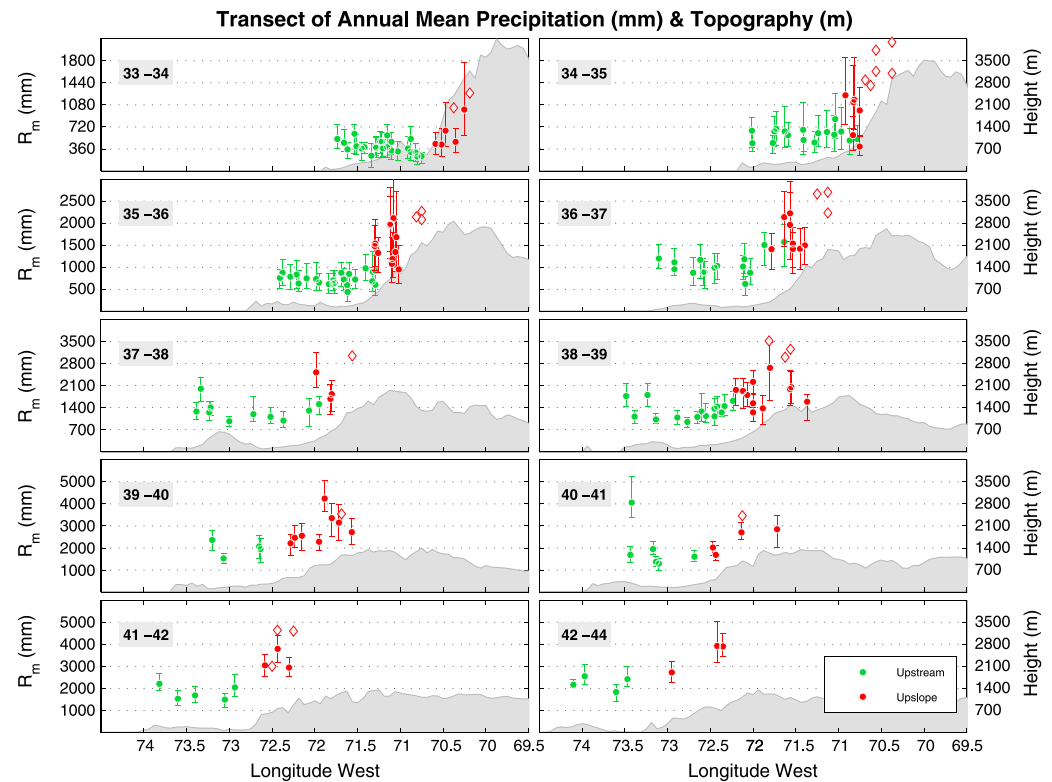


**Figure 4.** Transect of annual mean precipitation ( $R_m$  in millimeter) from the upstream to the upslope zone. The transects are  $1^\circ$  latitude width (except for the  $42^\circ\text{--}44^\circ$  transect due to data availability) and extend from the  $33^\circ\text{S}$  to the  $44^\circ\text{S}$ , where surface data were available. The circles correspond to the mean values and the bars to the minimum and maximum annual means over the 10 year (2002–2011) period, while the diamond correspond to the mean annual precipitation estimated from river discharge gauges on upslope sector. The east-west cross section of mean altitude (meter) is also shown by a gray area plot using GEOTOP30 data. See text for the definition of the limits to the different cross-barrier zones (upstream, upslope).

ratios over the subtropical Andes are in agreement with previous observational studies in that region [Falvey and Garreaud, 2007; Viale and Nuñez, 2011]. We further determined that the orographic enhancement ratios are rather similar in each year, and thus, a robust feature, as hinted by the maximum and minimum annual values over the 10 year record (i.e., the error bars in Figure 4).

A noteworthy aspect of this analysis is that the orographic enhancement ratio does not change significantly from the subtropical Andes to the extratropical Andes in spite of the significant change in mean height of the

**Table 1.** Areal Average of Annual Mean Precipitation and Enhancement Rates for Different Cross-Barrier Zones and for Different Latitudinal Bands of Figure 3<sup>a</sup>

Latitudinal Band	Areal Precipitation (mm) Over Each Cross-Barrier Zone		Enhancement Rates
	Upstream	Upslope	
$33^\circ\text{S}\text{--}34^\circ\text{S}$	395 (24)	758 (7)	1.92
$34^\circ\text{S}\text{--}35^\circ\text{S}$	595 (17)	1306 (12)	2.20
$35^\circ\text{S}\text{--}36^\circ\text{S}$	730 (23)	1650 (14)	2.26
$36^\circ\text{S}\text{--}37^\circ\text{S}$	1055 (15)	1923 (11)	1.82
$37^\circ\text{S}\text{--}38^\circ\text{S}$	1296 (10)	2266 (4)	1.75
$38^\circ\text{S}\text{--}39^\circ\text{S}$	1295 (15)	2148 (14)	1.66
$39^\circ\text{S}\text{--}40^\circ\text{S}$	1972 (4)	2942 (9)	1.49
$40^\circ\text{S}\text{--}41^\circ\text{S}$	1990 (6)	2542 (5)	1.28
$41^\circ\text{S}\text{--}42^\circ\text{S}$	1781 (5)	3663 (6)	2.06
$42^\circ\text{S}\text{--}44^\circ\text{S}$	2232 (4)	3309 (4)	1.48

<sup>a</sup>The number between parentheses represent the available stations from the daily data set over 2002–2011 period to calculate the areal average of each zone (see also Figure 1).



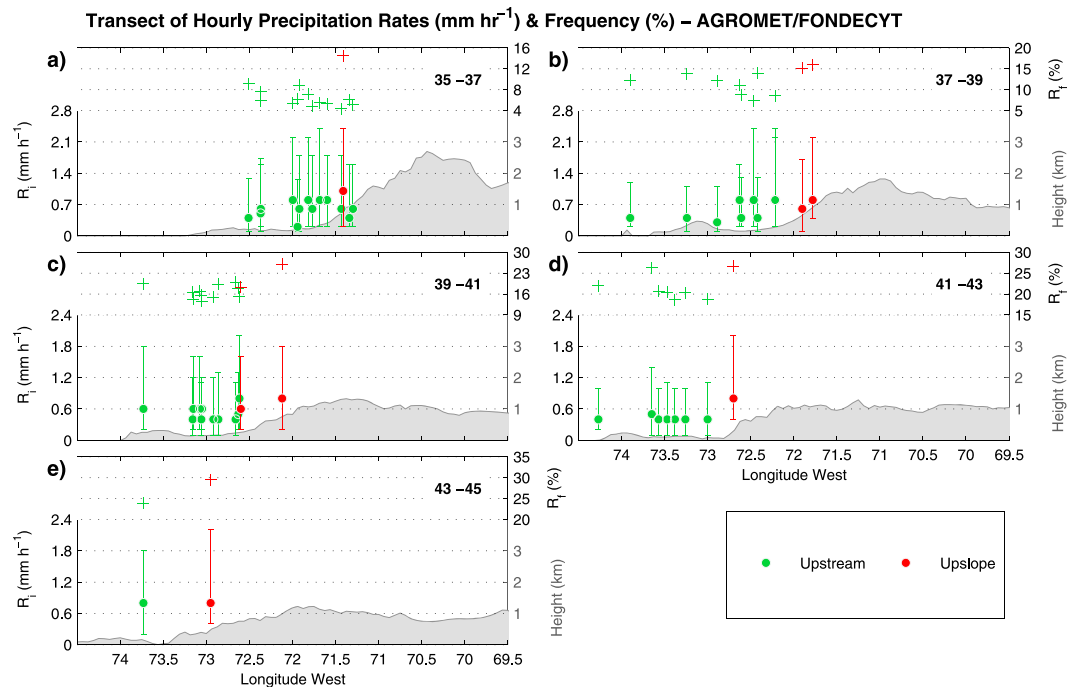


**Figure 5.** Transects of intensity ( $R_i$  in  $\text{mm h}^{-1}$ ) and frequency ( $R_f$  in %) of precipitation using hourly rain gauges data set for different cross-barrier zones from the upstream (green) to the upslope zone (red). The intensity of precipitation is presented by errorbars with the median (circles) and 25th and 75th percentile limits (barbs) values; while the frequency of precipitation is depicted with plus signs. The transects are 2° latitude width and extends from the 35°S to the 45°S.

Cordillera (and annual mean accumulation) from ~4000 m asl (~300 mm) at 33°S to less than 1500 m asl (~2000 mm) at 44°S. These ratios, however, must be taken with caution due to the low number of snow gauges (especially in the upslope zone), the presence of other topographic features, and deviations from the straight north-south orientation of the Andes. For example, the large ratio observed in the 35°–36°S latitudinal band could be the result of a slightly change in the north-south orientation of the Andes cordillera to a more perpendicular direction to the north-west winds; whereas the low ratios observed between 38°S and 41°S could be related to enhanced upstream precipitation over the elevated coastal range (up to 1000 m asl). A denser gauge network and advanced methods for grouping gauges [e.g., Daly *et al.*, 1994; Castro *et al.*, 2014] are needed to better represent spatial distribution of precipitation over complex terrain.

#### 4.2. Intensity and Frequency of Precipitation

Using the daily data set, we found that in each zonal transect, there is no increase in the frequency of rainy days from the coast to the mountains (not shown), so the increase in annual rainfall in the cross-mountain direction appears largely explained by an increase in daily “intensity” (not shown, but both discernible in Figures 3b and 3c). This characterization, however, could be misleading since a high daily accumulation can be caused by a short period of high-intensity rainfall or a higher frequency of low-intensity rainfall. This caveat has been already pointed out by Biassutti and Yuter [2013] using instantaneous rainfall estimates from Tropical Rainfall Measuring Mission (TRMM) satellite and surface daily precipitation data over tropical latitudes, so we now turn to our hourly data set.

The cross-barrier variation in hourly intensity (median and 25th and 75th percentile limits of  $R_i$  in  $\text{mm h}^{-1}$ ) and frequency ( $R_f$  in %) is displayed in Figure 5. The number of rain gauges available for this analysis is substantially reduced, so we considered zonal transects of 2° of latitude. In all transects,  $R_f$  as well as the median and 25th and 75th percentile values of  $R_i$ , are higher in the easternmost (upslope) stations than those in the westernmost stations (near the coastline). The rain frequency increases from the westernmost to the easternmost station by a factor between 4% and 10%. Recall that the Andes deviates slightly from its north-south orientation between 34°S and 37°S (Figure 1), so some upstream stations locate to the east

**Table 2.** Frequency (%) of Rainy Profiles Observed Over the Entire Year by Cloudsat Satellite Data for Different Cross-Barrier Zones and Different Latitudinal Bands Over the ~8 Year Period (2007–2014)

Latitudinal Band	Frequency (%) of Rainy Profiles From CloudSat Satellite Data Over Each Cross-Barrier Zone			
	Open Ocean	Costal	Upstream	Upslope
30°S–35°S	1.9%	1.0%	1.4%	5.6%
35°S–40°S	4.9%	6.7%	8.6%	11.4%
40°S–45°S	10.7%	12.9%	16.3%	25.0%
45°S–50°S	13.6%	19.5%	33.6%	33.1%
50°S–55°S	18.4%	27.1%	38.8%	36.1%

of the only upslope station within the 35°S–37°S transect (Figure 5a). As noted before, the frequency of rainy days exhibits no increase toward the mountains, so the increase in hourly  $R_f$  indicates that subdaily rainy events over the upslope zone tend to last longer than those over the upstream and costal zones (due to an earlier onset or later demise). The increase in subdaily rain frequency from the Pacific Ocean to the upslope zone is corroborated by the instantaneous estimates over the entire year period from the CloudSat data (Table 2), which additionally suggest that the increase in  $R_f$  over the Andes' windward side is more accentuated between 30°S and 35°S (i.e., the tallest sector) than farther south. Likewise, the median of  $R_i$  increases between 0.3 mm/h and 0.8 mm/h from the westernmost to the easternmost rain gauge station. Indeed, when considering all the stations in each transect, the cross-barrier variation of  $R_f$  and  $R_i$  is disperse, but the easternmost station in the upslope zone always exhibits the largest values. Therefore, the orographic enhancement of precipitation amount along the Andes results from both higher subdaily precipitation frequency and intensity over the mountains relative to their counterparts at lower elevations.

## 5. Orographic Effects on Upwind Precipitating Cloud Inferred From Satellite Data

In order to obtain robust statistics of precipitating stratiform clouds, only rainy profiles observed between March and November were considered here. We have excluded summer profiles—presumably affected by deep convection—although using the whole sample does not change substantially our results given the small fraction of convective precipitation in the western subtropical Andes [Viale and Garreaud, 2014].

Let us begin our analysis with the macrophysical properties of precipitating clouds. Figure 6 shows the depth of cloud layers and the freezing level in each cross-barrier zone within the 5° of latitude zonal bands (see Figure 1). Since 2B-GEOPROF-LIDAR data do not make distinction between cloud and precipitation, the depth of rainy cloud layers was estimated as the difference between the cloud top height and the surface elevation, in the case of a single-layer cloud in the profile. For multilayer clouds (20%–25% of all rainy profiles), the depth was calculated as the sum of the successive cloud layer depths. The freezing level was obtained from the European Centre for Medium-Range Weather Forecasts (ECMWF)-AUX CloudSat product, which contains interpolated data to each CPR profile from a data set provided by the European Center for Medium-Range Weather Forecasts.

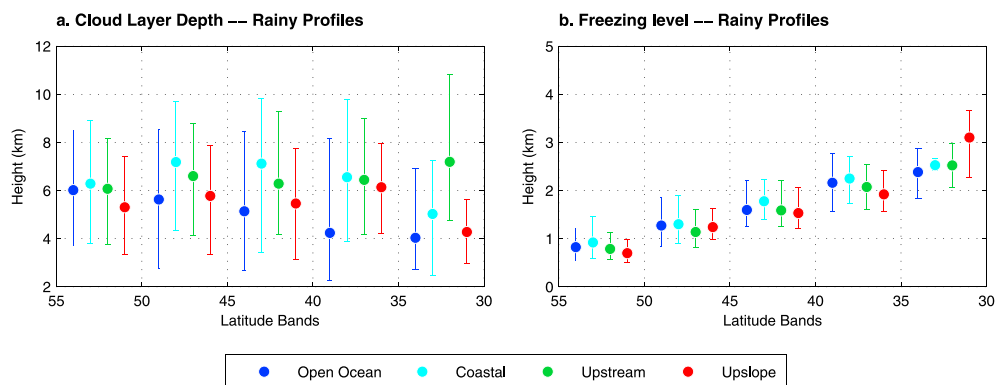


**Figure 6.** (a) Cloud layer depth and (b) freezing level for rainy profiles for different latitude bands and cross-barrier zones. The circles correspond to the median values and the bars to the 25th and 75th percentile limits.



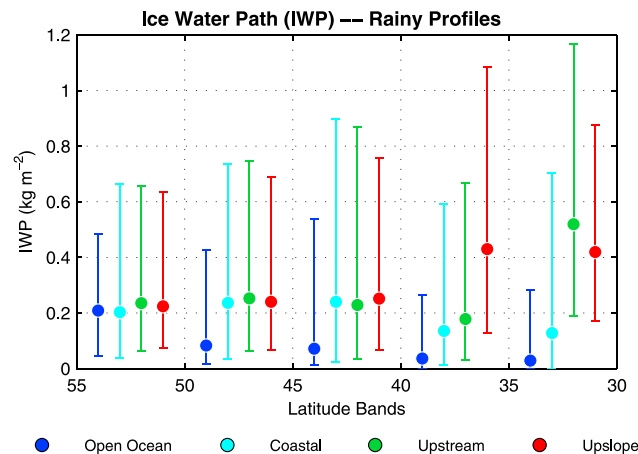


**Figure 7.** Ice water path (IWP in  $\text{kg m}^{-2}$ ) for the  $5^\circ$  wide latitudinal bands and the different cross-barrier zones. The circles correspond to the median values and the bars to the 25th and 75th percentile limits.

The cloud depth values in the coastal, upstream, and upslope sectors do not change much with latitude, in contrast with the cloud depth over the open ocean that becomes gradually thinner toward the subtropics (Figure 6a). The cloud depths reduce from the coast to the mountains, gradually to the south of  $35^\circ\text{S}$ , and more intermittently to the north of  $35^\circ\text{S}$ . To the south of  $35^\circ\text{S}$ , the cloud depth is  $>5$  km and largely cold as the freezing level ranges from 1 to 2 km asl when precipitation occurs (Figure 6b). The gradually lowering of the freezing level from the coast to the mountains further suggests that cold rain process may dominate, since this behavior has been associated with

the latent cooling from the melting of orographically enhanced frozen precipitation and with pseudo adiabatic cooling produced by lifting [Minder *et al.*, 2011; Minder and Kingsmill, 2013].

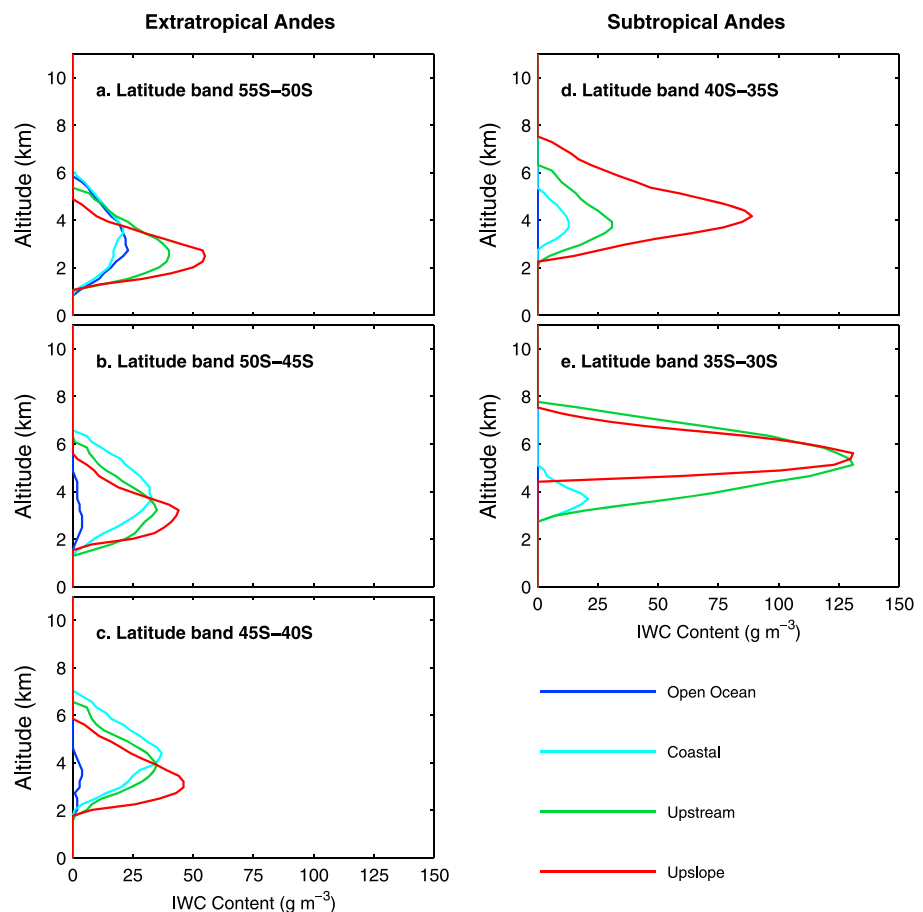


**Figure 8.** Vertical profiles of ice water content (IWC in  $\text{g m}^{-3}$ ) for different  $5^\circ$  wide latitudinal bands: (a)  $55^\circ\text{S}$ – $50^\circ\text{S}$ , (b)  $50^\circ\text{S}$ – $45^\circ\text{S}$ , (c)  $45^\circ\text{S}$ – $40^\circ\text{S}$ , (d)  $40^\circ\text{S}$ – $35^\circ\text{S}$ , and (e)  $35^\circ\text{S}$ – $30^\circ\text{S}$ . The different colors denote the different cross-barrier zones. The vertical profiles show the median values of IWC at each vertical level for only the profiles classified as rainy according to the 2C-PRECIP CloudSat product.

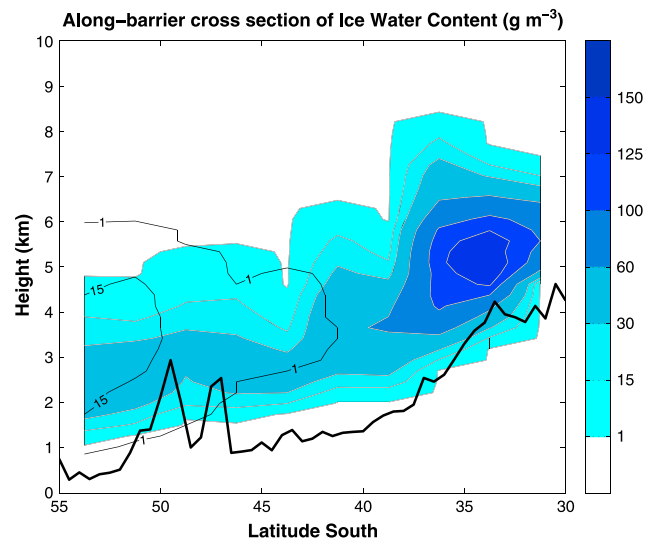


**Figure 9.** Vertical section in along-barrier direction showing the median values of ice water content (IWC) of rainy profiles from the CWC-RO CloudSat data over the open ocean (lines) and the upslope (shaded) cross-barrier zones. For the definition of open ocean and upslope cross-barrier zones, see text. The black thick line shows the crest altitude of the Andes averaged within  $0.5^\circ$  wide latitude band (see Figure 1). IWC lines contour of 1, 15, 30, 60, 100, 125, and  $150 \text{ g m}^{-3}$  are plotted, when are present, for both cross-barrier zones.

To the north of  $35^\circ\text{S}$ , the cloud depth is relatively thick ( $>4 \text{ km}$ ) and the freezing level ranges from 2.5 to 3 km, so cold rain process seems to also dominate there (Figure 6). In contrast to midlatitudes, here the freezing level rises from the upwind zones (lower terrain) to the windward slope (higher terrain). Over the lower terrain, rainy events occur mostly during winter under cold conditions. Over the higher terrain, rainy events concentrate during winter but also occur during fall and spring (see Table 2). Rainy events during the transition seasons are accompanied by warmer conditions and contribute to a higher average freezing level. Indeed, if we restrict our averaging period to winter, the freezing level over the upslope sector is lower than over the upwind sectors.

Given the cold, stratiform nature of midlatitude precipitation systems, where the ice particles grow aloft (by vapor diffusion, aggregation, and rimming)

and precipitate [e.g., Houze, 1993], we now focus on describing cross-barrier variations of ice water content (IWC) and its vertical integral (ice water path (IWP)) within the clouds. Indeed, observational studies using CloudSat data have recently quantified that cold rain process dominates in frontal systems over the northeastern Pacific Ocean, especially to north of  $40^\circ\text{N}$ , and also produces higher rain rates than warm rain process [Matrosov, 2012, 2013]. Moreover, warm stratiform clouds (tops below  $0^\circ\text{C}$  isotherm) produce light rain and are only relevant over the subtropical offshore zones.

Figure 7 shows the median, 25th and 75th percentiles of the IWP when rain is present for the cross-barrier zones within each of the  $5^\circ$  latitude zonal bands (see Figure 1). Similar to the cloud depth, the total ice within clouds reduces gradually equatorward over the open ocean. To the south of the  $50^\circ\text{S}$ , the ice content change little from open ocean to the upslope of the Austral Andes (about  $0.2 \text{ kg m}^{-2}$ ). Between  $50^\circ\text{S}$  and  $40^\circ\text{S}$ , the IWP increases from the open ocean to coastline and then it remains relatively constant over the coastal, upstream, and upslope sectors. In contrast, to the north of  $40^\circ\text{S}$ , there is a marked increase in IWP from the ocean ( $\text{IWP} < 0.05 \text{ kg m}^{-2}$ ) to the Andes ( $\text{IWP} > 0.4 \text{ kg m}^{-2}$ ). Somewhat surprisingly, the IWP over the upslope of the subtropical Andes is twice as large as its counterpart over the extratropical Andes.

Further microphysical information is gained from the vertical profiles of IWC at the different cross-barrier zones within the  $5^\circ$  latitude zonal bands (Figures 8 and 9). Each profile represents the median values of IWC in each vertical bin of 250 m deep. To the south of  $50^\circ\text{S}$  (Figure 8a), the maximum IWC over the upslope zone is larger than the maximum offshore, but as commented before, the cloud becomes thinner toward the mountains (Figure 6a) so IWP varies little in the cross-barrier direction (Figure 7). Also note that the level of maximum IWC moves downward as one move toward the mountain, indicative of an augmented size of the ice particles just above the freezing level, since ice number concentration (INC) (in the 2B-CWC-RO product, not shown) maximum and total ice mass (IWP) remain similar among all cross-barrier zones. Between  $50^\circ\text{S}$  and  $40^\circ\text{S}$  (Figures 8b and 8c), there is little ice in the clouds over the ocean and the IWC maximum moves downward gradually from the coast to the Andes. A substantially different behavior is observed to the north of  $40^\circ\text{S}$  (Figures 8d and 8e), where the ice content is almost absent in clouds over the open ocean zone (indicative of warm rain processes), slightly larger over the coastal zone,

and considerably enhanced in clouds close to and over the Andes. In the transect of 30°S–35°S (highest Andean elevation), the continental upstream IWC profile is very similar to the profile over the upslope (Figure 8e), denoting a prominent upstream orographic effect on precipitating clouds. Overall, cross-barrier and along-barrier variations in IWC observed to the north of 50°S (Figure 8) are closely related to variations in IWP (Figure 7) and the number of ice particles (i.e., INC not shown), suggesting an augmented density and mass of ice clouds (rather than an augmented size of ice particles).

## 6. Discussion

The vertical section of IWC in the along-barrier direction (Figure 9) further illustrates the accentuated orographic effect of the subtropical Andes compared to that at the extratropical Andes on increasing ice content within clouds. The IWC maximum over the windward slopes of the subtropical Andes ( $\sim 70\text{--}120\text{ g/m}^3$ ) is quite larger and occurs at considerably higher levels (5–6 km) than its counterpart over the extratropical Andes ( $\sim 40\text{ g/m}^3$  at 2–3 km). Conversely, the IWC maximum over the subtropical Ocean ( $\sim 1\text{ g/m}^3$ ) is much less than its counterpart over the extratropical Ocean ( $\sim 20\text{ g/m}^3$ ). Such contrasting microphysical behavior of the upwind precipitating clouds between subtropical and extratropical latitudes calls for plausible physical explanations that we offer below. A full understanding of the interplay between topography, synoptic forcing (e.g., impinging winds), and microphysics is beyond the scope of this paper as it requires further observational data combined with modeling results.

A first possibility to explain IWP differences along the Andes is latitudinal changes in the ice nuclei (IN) arriving to the west coast of South America. Available climatologies of the cloud condensation nuclei (CCN) [Spracklen *et al.*, 2011; Karydis *et al.*, 2011] give a rough estimation of the IN distribution and show a transition from very clean air masses over Pacific to the south of 40°S to more polluted conditions at subtropical latitudes. Nevertheless, the equatorward increase in CCN concentration is in a factor of 2–4, so it may hardly explain the variations in IWP found in our study.

Second, given the north-south variations in the height of the Andes (taller at the subtropics) and synoptic forcing (stronger in the extratropics), there could be changes in the dynamic flow regimes (unblocked and blocked flows) impinging the mountains and their effect on precipitation. To the south of 40°S, the Andes are lower than 1500 m asl and the winds are stronger, leading to more favorable unblocked conditions that enhance clouds and precipitation directly over the windward slopes of the barrier [e.g., Medina and Houze, 2003]. However, under stable stratification and strong wind conditions, the orographic lifting can trigger vertically propagating gravity waves, enhancing ice clouds well upstream of the barrier even in unblocked conditions [Reinking *et al.*, 2000; Colle, 2004]. The terrain-blocked flow dynamics may also contribute on cloud ice enhancement upstream of the low extratropical Andes, since it has been documented operating in advance of the relatively low coastal Californian ranges [Neiman *et al.*, 2004; James and Houze, 2005]. Plausible microphysical processes operating in clouds over the extratropical Andes are also insinuated from our results. The gradual increase and lowering of the IWC maximum in the vertical profiles, and the decrease in cloud thickness toward the Andes, suggest that turbulent cells could accelerate the growth and fallout of ice particles by riming and aggregation over the mountainous coastline and the windward slopes of the Andes [e.g., Garvet *et al.*, 2007; Houze and Medina, 2005; Medina *et al.*, 2007].

Several studies have shown that a blocked flow regime characterizes winter storm reaching the subtropical Andes [Falvey and Garreaud, 2007; Barrett *et al.*, 2011; Viale and Nuñez, 2011]. In this regime, the terrain-induced upward motion and gravity waves can start far in advance of the barrier, and consequently, the orographic precipitation enhancement expands well upstream of the barrier [e.g., Houze *et al.*, 2001; Bousquet and Smull, 2003]. Idealized simulations performed by Galewsky [2008] revealed that upstream low-level blocked flow triggers vertically propagating gravity waves, and its upward motion component can produce substantial amounts of cloud ice far upstream of the barrier, constituting seeder ice particles at upper levels and a potential for upstream precipitation enhancement. Such seeder-feeder mechanism has been proposed as responsible for far upstream-enhanced precipitation linked to an intense frontal system approaching the subtropical Andes [Viale *et al.*, 2013], and therefore, it offers a sound physical interpretation for largely enhanced upstream cloud ice observed upstream of the subtropical Andes in this study.

## 7. Conclusions

Stratiform precipitation from midlatitude frontal systems falls over the western coast of southern South America being profoundly altered as they approach and move over the elevated terrain of the Andes. The orographic effects of the Andes at subtropical (30°S–40°S, mean height > 3 km) and extratropical (40°S–55°S, mean height < 1.5 km) latitudes on windward-side rainfall and precipitating clouds have been investigated using surface (daily and hourly rain gauge data) and CloudSat satellite data.

The annual mean precipitation along the Andes foothills increases from ~300–500 mm at subtropical latitudes to >2000 mm to the south of 40°S, largely a consequence of a southward increase in the frequency of rainy events. Superimposed in that marked latitudinal variation, the annual mean precipitation increases from the low upstream terrain to the windward slopes of the Andes by a factor between 1.3 and 2.3. In spite of the low station density and the existence of low coastal topographic features, the long-term precipitation ratios indicate a consistent Andean orographic enhancement in all sampled latitudes (from 33°S to 44°S), in agreement with previous observational studies in the subtropical region [Falvey and Garreaud, 2007; Viale and Nuñez, 2011]. The hourly precipitation data and the instantaneous satellite estimates indicate that the orographic enhancement of the annual precipitation responds to a cross-barrier increase of both the intensity and frequency of rainy events. The higher frequency of hourly rainy events over the higher terrain is mostly consequence of longer duration of rainstorms at hourly time scales. No such frequency increase is found when considering daily time scales.

Overall, the climatological results from CloudSat data indicate that the precipitating clouds are enhanced upstream of both the extratropical and subtropical Andes. These results closely agree with the findings of Falvey and Garreaud [2007] and Barrett *et al.* [2011] obtained from Special Sensor Microwave/Imager and TRMM satellite data (see their both Figure 2) and thus strongly suggest that upstream orographic precipitation enhancement occurs along most of the west coast of the southern South America (30°S–50°S). The CloudSat satellite data suggest that the orographic effects of the Andes on upwind precipitating clouds increase gradually from midlatitudes to the subtropics, a result that likely is a function of a gradual reduction of synoptic-scale forcing and an increase of the altitude of the barrier equatorward. In midlatitudes, strong synoptic-scale winds and frontal-scale ascent produce deep (>5 km) and cold precipitating clouds everywhere, which in turn, lead to moderate orographic effects of the low Andes on clouds. In the subtropics, a weak synoptic-scale forcing produces shallow and warm precipitating clouds offshore but is strong enough to produce a strong orographic effect of the tall Andes on precipitating clouds.

However, a better assessment of dynamical and microphysical processes operating over the Andes requires further analyses. Future studies should be aimed at dealing with upstream blocking or unblocked dynamics conditions and mountain gravity waves leading to the observed upstream orographic cloud ice enhancement, using detailed in situ observations and numerical simulations, as well as determine microphysical processes operating within precipitating clouds, especially in the vicinity of the remote and unrepresented extratropical Andes.

## Acknowledgments

This research was supported by FONDECYT 3130688 and FONDAP CR2. Rain gauge data were obtained from the Red Agroclimática Nacional (AGROMET) and Dirección General de Aguas (DGA) de Chile. We are grateful to El Chacay and Andean Rose lodgings, Carabineros de Chile, INDAP-Chaiten, staff of the Chilean National Park (CONAF) in Cucao and Mocha Island, and National Weather Service (DMC) in Temuco, Osorno, and Melinka for taking care of the weather stations, and to Marcelo Ibarra for managing the data. CloudSat data were obtained from the CloudSat Data Processing Center ([www.cloudsat.cira.colostate.edu](http://www.cloudsat.cira.colostate.edu)). We also acknowledge the detailed and insightful comments from the reviewers which largely improved our manuscript.

## References

- Austin, R. T., A. J. Heymsfield, and G. L. Stephens (2009), Retrieval of ice cloud microphysical parameters using the CloudSat millimeter-wave radar and temperature, *J. Geophys. Res.*, *114*, D00A23, doi:10.1029/2008JD010049.
- Barrett, B. S., R. D. Garreaud, and M. Falvey (2009), Effect of the Andes cordillera on precipitation from a midlatitude cold front, *Mon. Weather Rev.*, *137*, 3092–3109.
- Barrett, B. S., D. B. Krieger, and C. P. Barlow (2011), Multiday circulation and precipitation climatology during winter rain events of differing intensities in Central Chile, *J. Hydrometeorol.*, *12*, 1071–1085.
- Biasutti, M., and S. E. Yuter (2013), Observed frequency and intensity of tropical precipitation from instantaneous estimates, *J. Geophys. Res. Atmos.*, *118*, 9534–9551, doi:10.1002/jgrd.50694.
- Bousquet, O., and B. F. Smull (2003), Observations and impacts of upstream blocking during a widespread orographic precipitation event, *Q. J. R. Meteorol. Soc.*, *129*, 391–409.
- Castro, L. M., J. Gironás, and B. Fernández (2014), Spatial estimation of daily precipitation in regions with complex relief and scarce data using terrain orientation, *J. Hydrol.*, *517*, 481–492.
- Colle, B. (2004), Sensitivity of orographic precipitation to changing ambient conditions and terrain geometries: An idealized modelling perspective, *J. Atmos. Sci.*, *61*, 588–606.
- Daly, C., R. P. Neilson, and D. L. Phillips (1994), A statistical-topographic model for mapping climatological precipitation over mountainous terrain, *J. Appl. Meteorol.*, *33*(2), 140–158.
- Falvey, M., and R. Garreaud (2007), Wintertime precipitation episodes in Central Chile: Associated meteorological conditions and orographic influences, *J. Hydrometeorol.*, *8*, 171–193.

- Frei, C., and C. Schär (1998), A precipitation climatology of the Alps from high-resolution rain gauge observations, *Int. J. Climatol.*, **18**, 873–900.
- Galewsky, J. (2008), Orographic clouds in terrain-blocked flows: An idealized modeling study, *J. Atmos. Sci.*, **65**, 3460–3478.
- Garreaud, R. D. (2013), Warm winter storms in Central Chile, *J. Hydrometeorol.*, **14**, 1515–1534.
- Garreaud, R. D., P. Lopez, M. Minvielle, and M. Rojas (2013), Large-scale control on the Patagonian climate, *J. Clim.*, **26**, 215–230.
- Garreaud, R. D., M. G. Nicora, R. E. Bürgesser, and E. E. Ávila (2014), Lightning in western Patagonia, *J. Geophys. Res. Atmos.*, **119**, 4471–4485, doi:10.1002/2013JD021160.
- Garvet, M. F., B. Smull, and C. Mass (2007), Multiscale mountain waves influencing a major orographic precipitation event, *J. Atmos. Sci.*, **64**, 711–737.
- Haynes, J. M., T. S. L'Ecuyer, G. L. Stephens, S. D. Miller, C. Mitrescu, N. B. Wood, and S. Tanelli (2009), Rainfall retrieval over the ocean with spaceborne W-band radar, *J. Geophys. Res.*, **114**, D00A22, doi:10.1029/2008JD009973.
- Hoskins, B. J., and K. I. Hodges (2005), A new perspective on Southern Hemisphere storm tracks, *J. Clim.*, **18**, 4108–4129.
- Houze, R. A., Jr. (1993), *Cloud Dynamics*, Academic Press, San Diego, Calif.
- Houze, R. A., Jr. (2012), Orographic effects on precipitating clouds, *Rev. Geophys.*, **50**, RG1001, doi:10.1029/2011RG000365.
- Houze, R. A., Jr., and S. Medina (2005), Turbulence as a mechanism for orographic precipitation enhancement, *J. Atmos. Sci.*, **62**, 3599–3623.
- Houze, R. A., Jr., N. C. James, and S. Medina (2001), Radar observations of precipitation and airflow on the Mediterranean side of the Alps: Autumn 1998 and 1999, *Q. J. R. Meteorol. Soc.*, **127**, 2537–2558.
- Im, E., C. L. Wu, and S. L. Durden (2005), Cloud profiling radar for CloudSat mission, *IEEE Aero. Electron. Syst. Mag.*, **20**, 15–18.
- James, C. N., and R. A. Houze Jr. (2005), Modification of precipitation by coastal orography in storms crossing northern California, *Mon. Weather Rev.*, **133**, 3110–3131.
- Karydis, V. A., P. Kumar, D. Barahona, I. N. Sokolik, and A. Nenes (2011), On the effect of dust particles on global cloud condensation nuclei, *J. Geophys. Res.*, **116**, D23204, doi:10.1029/2011JD016283.
- Lenaerts, J., M. Van den Broeke, J. Van Wessel, W. Van de Berg, E. Van Meijgaard, L. Van Ulf, and M. Schaefer (2014), Extreme precipitation and climate gradients in Patagonia revealed by high-resolution regional atmospheric climate modelling, *J. Clim.*, **27**, 4607–4621.
- Mace, G. G., R. Marchand, Q. Zhang, and G. Stephens (2007), Global hydrometeor occurrence as observed by CloudSat: Initial observations from summer 2006, *Geophys. Res. Lett.*, **34**, L09808, doi:10.1029/2006GL029017.
- Mace, G. G., Q. Zhang, M. Vaughan, R. Marchand, G. Stephens, C. Trepte, and D. Winker (2009), A description of hydrometeor layer occurrence statistics derived from the first year of merged Cloudsat and CALIPSO data, *J. Geophys. Res.*, **114**, D00A26, doi:10.1029/2007JD009755.
- Marchand, R., G. G. Mace, T. Ackerman, and G. Stephens (2008), Hydrometeor detection using CloudSat—An Earth-orbiting 94-GHz cloud radar, *J. Atmos. Oceanic Technol.*, **25**, 519–533.
- Matrosov, S. Y. (2012), Observation of wintertime U.S. west coast precipitating systems with W-Band satellite radar and other spaceborne instrument, *J. Hydrometeorol.*, **13**, 223–238.
- Matrosov, S. Y. (2013), Characteristics of landfalling atmospheric rivers inferred from satellite observations over the eastern North Pacific Ocean, *Mon. Weather Rev.*, **141**, 3757–3768.
- Medina, S., and R. A. Houze Jr. (2003), Air motions and precipitation growth for orographic precipitation enhancement, *Q. J. R. Meteorol. Soc.*, **129**, 345–371.
- Medina, S., E. Sukovich, and R. A. Houze Jr. (2007), Vertical structures of precipitation in cyclones crossing the Oregon Cascades, *Mon. Weather Rev.*, **135**, 3565–3586.
- Minder, J. R., and D. E. Kingsmill (2013), Mesoscale variations of the atmospheric snowline over the Northern Sierra Nevada: Multiyear statistics, case study, and mechanisms, *J. Atmos. Sci.*, **70**, 916–938.
- Minder, J. R., D. L. Durran, and G. H. Roe (2011), Mesoscale controls on the mountainside snowline, *J. Atmos. Sci.*, **68**, 2107–2127.
- Neiman, P. J., F. M. Ralph, A. B. White, D. A. Kingsmill, and P. O. G. Persson (2002), The statistical relationship between upslope flow and rainfall in California's coastal mountains: Observations during CALJET, *Mon. Weather Rev.*, **130**(1468), 1492.
- Neiman, P. J., P. O. G. Persson, F. M. Ralph, D. P. Jorgensen, A. B. White, and D. A. Kingsmill (2004), Modification of fronts and precipitation by coastal blocking during an intense landfalling winter storm in southern California: Observations during CALJET, *Mon. Weather Rev.*, **132**, 242–273.
- Neiman, P. J., A. B. White, F. M. Ralph, D. J. Gottas, and S. I. Gutman (2009), A water vapor flux tool for precipitation forecasting, *J. Water Manage.*, **162**, 83–94.
- Pierrehumbert, R. T., and B. Wyman (1985), Upstream effects of mesoscale mountains, *J. Atmos. Sci.*, **42**, 977–1003.
- Rasmussen, L. A., and W. V. Tangborn (1976), Hydrology of the North Cascades region, Washington: 1. Runoff, precipitation, and storage characteristics, *Water Resour. Res.*, **12**(2), 187–202, doi:10.1029/WR012i002p00187.
- Reinking, H. D., J. B. Snider, and J. L. Coen (2000), Influences of storm-embedded orographic gravity waves on cloud liquid water and precipitation, *J. Appl. Meteorol.*, **39**, 733–759.
- Roe, G. H. (2005), Orographic precipitation, *An. Rev. Earth Planet. Sci.*, **33**, 645–671.
- Rotunno, R., and R. Ferretti (2001), Mechanisms of intense Alpine rainfall, *J. Atmos. Sci.*, **58**, 1732–1749.
- Rutllant, J., and H. Fuenzalida (1991), Synoptic aspects of the Central Chile rainfall variability associated with the southern oscillation, *Int. J. Climatol.*, **11**, 63–76, doi:10.1002/joc.3370110105.
- Smith, R. B., and J. P. Evans (2007), Orographic precipitation and isotope fraction over the southern Andes, *J. Hydrometeorol.*, **8**, 3–14.
- Spracklen, D. V., K. S. Carslaw, U. Pöschl, A. Rap, and P. M. Forster (2011), Global cloud condensation nuclei influenced by carbonaceous combustion aerosol, *Atmos. Chem. Phys.*, **11**, 9067–9087.
- Stephens, G. L., et al. (2002), The CloudSat mission and the A-train: A new dimension of space-based observations of clouds and precipitation, *Bull. Am. Meteorol. Soc.*, **83**, 1771–1790.
- Viale, M., and R. D. Garreaud (2014), Summer precipitation events over the western slopes of the subtropical Andes, *Mon. Weather Rev.*, **142**, 1074–1092.
- Viale, M., and M. N. Nuñez (2011), Climatology of winter orographic precipitation over the subtropical Central Andes and associated synoptic and regional characteristics, *J. Hydrometeorol.*, **12**, 481–507.
- Viale, M., R. A. Houze Jr., and K. L. Rasmussen (2013), Upstream orographic enhancement of a narrow coldfrontal rainband approaching the Andes, *Mon. Weather Rev.*, **141**, 1708–1730.
- Winker, D. M., M. A. Vaughan, A. H. Omar, Y. Hu, K. A. Powell, Z. Liu, W. H. Hunt, and S. A. Young (2009), Overview of the CALIPSO mission and CALIOP data processing algorithms, *J. Atmos. Oceanic Technol.*, **26**, 2310–2323.
- Yuter, S. E., D. A. Stark, J. A. Crouch, and M. J. Payne (2011), The impact of varying environmental conditions on the spatial and temporal patterns of orographic precipitation over the Pacific Northwest near, Portland, Oregon, *J. Hydrometeorol.*, **12**, 330–351.